Vol.4, No.6, Page 2254- 2264, 2026 https://doi.org/10.59628/jast.v4i6.2827 ISSN 2958-9568 JAST

SUN PUBLISHER

مجلة جامعة صنعاء للعلوم التطبيقية والتكنولوجيا

Sana'a University Journal of Applied Sciences and Technology

https://journals.su.edu.ye/index.php/jast/

Effect of the Cu additions on the structure of the soldered (96.5- x)Sn - (3.5)Ag -(x)Cu alloy with x=0.2, 0.4, 0.6, 0.8 and 1 wt %

Amtalsabowr A.AL-Thamari[1,2], A.H.Al-Hammadi[1], Ibrahim G.H. Loqman[1] * and Ahmed.M.A.Haider[1]

[1] **Department of Physics, Faculty of Sciences, Sana'a University, Sana'a, Yemen,**
[2] **Department of Physics, Faculty of Education, Al-Mahweet University, Al-Mahweet, Yemen.**

*Corresponding author: i.luqman@su.edu.ye

Abstract

The microstructural characteristics of solder alloys critically determine their mechanical performance and reliability in high-precision electronic applications. These characteristics including phase distribution, grain size, and intermetallic compound (IMC) formation govern the alloy's response to thermal and mechanical stresses. Precise control of IMCs such as Cu_6Sn_5 and Ag_3Sn, along with uniform fine grains, enhances toughness, creep resistance, and reduces fracture susceptibility. In this study, the effect of low copper additions (0.2–1 wt %) on the (96.5- x) $Sn-3.5Ag-xCu$ alloy was systematically investigated through a combination of XRD and SEM analyses. The results reveal a clear dependence of crystallite size, dislocation density, and IMC distribution on copper content and identify the optimal Cu concentration for stabilizing the β -Sn phase while improving mechanical properties. These findings provide a detailed understanding of microstructural evolution under low-Cu alloying, offering insights not addressed in previous studies.

Article Info

Keywords:
solder, lead-free, XRD, Eutectic , Sn-3.5Ag-Cu solder Alloy, SEM.

Article History:
Received: 06-February-2026,
Revised: 19-April-2026,
Accepted: 29-May-2026,
Published: 28 June 2026.

1. INTRODUCTION

Solders are required to assemble electronic components on printed circuit boards and ensure the reliability of electronic equipment. The Hazardous Substances Directive demands the removal of lead from solder connections, affecting the design and manufacture of electronic equipment. The Sn-Ag-Cu ternary system is becoming a preferred alternative to classic eutectic Sn-Pb solder alloys in electrical connection and packaging applications [1].

Sn-Pb solder alloys are widely used in the electronics industry because of their excellent combination of corrosion resistance, low melting temperature, low cost, wettability, and mechanical properties [2].

Eutectic Sn-Pb solder is a strong joining material used in the microelectronics sector. Many nations have regulated the use of lead in consumer electronics because of environmental concerns. This has prompted the search for other materials [3].

Sn-3.5Ag eutectic solder and its tertiary alloys are among the leading competitors. However, research on their creep and fatigue properties is limited. Sn-3.5Ag alloys outperform Pb-Sn eutectic solders in terms of melting point, IMC growth rate, and Cu dissolution rate. It was discovered that adding Cu to the Sn-3.5Ag alloy decreased the dissolution rate.

The Cu pad is used to boost the development rate of the IMC [4].

The selection of low copper concentrations is primarily attributed to their ability to induce controlled lattice distortion and promote grain refinement without causing excessive internal stress or the formation of coarse intermetallic compounds. At low concentrations, Cu contributes to improving microstructural homogeneity and enhances the formation of fine, uniformly distributed Cu_6Sn_5 particles, whereas increasing the Cu content may lead to

microstructural coarsening and a deterioration in mechanical reliability.

The ten-silver-copper (Sn-Ag-Cu) solder alloy exhibits a reduced corrosion susceptibility compared to the typical Sn-Pb solder in (0.1 mol) NaCl solution, which is associated with the formation of a more compact passive coating on the surface of the Sn-Ag-Cu solder alloy [5].

The alloy composition and various processing parameters, including the soldering temperature, cooling rate, and thermal treatment time, influence the microstructural development of the solder junction. These parameters influence the phase distribution, grain size, and intermetallic compound production, all of which have a direct impact on mechanical qualities such as strength, hardness, and resistance to delamination and cracking [6, 7].

Understanding the microstructural features of the Sn-Ag-Cu ternary system is essential for determining the mechanical performance and dependability of Sn-Ag-Cu solders. These characteristics assist designers and manufacturers in selecting the appropriate solder alloy for a specific application. This has the potential to be widely employed in electronic interconnections and packaging applications.

The purpose of this study was to examine the microstructures of five Sn-Ag-Cu solder alloys with varying Cu percentage [8, 9].

Previous studies on Sn–Ag–Cu alloys have primarily relied on X-ray diffraction (XRD) to identify crystalline phases such asβ-Sn, AgSn, and Cu_6Sn_5, and scanning electron microscopy (SEM) to describe the microstructure and distribution of intermetallic compounds. However, the use of XRD has remained largely qualitative, without a detailed quantitative analysis of lattice parameter variations and lattice distortions, while SEM analysis has been mainly descriptive and lacks a direct correlation with atomic-scale changes.

Accordingly, a scientific gap exists in the absence of a quantitative and physically based relationship linking XRD peak shifts and variations in the lattice parameters of the β-Sn phase to the microstructural evolution. This work addresses this gap by adopting a multi-scale approach that correlates Cu-induced lattice distortion with microstructural evolution, thereby providing a deeper understanding of the behavior of Sn–Ag–Cu alloys beyond the conventional phase-identification approach.

1.1. X-Ray Diffraction and Bragg's Law:

X-ray diffraction (XRD) is a technique used to identify the crystalline phases in materials and determine their lattice parameters. The XRD patterns provide insights into the atomic arrangement and crystallite size of the alloy. This study explored the impact of adding Cu to Sn-Ag solder alloys and examined how the composition of the alloy influences the crystallization process [10].

When a crystal is irradiated with X-rays of a given wavelength (λ) at an incidence angle (θ), the X-rays can either pass through the crystal or interact with specific atoms in the lattice. In reality, X-ray photons interact with the electron density around atoms, resulting in diffraction.

The rays reflected from adjacent planes have a path difference of 2dsinθ. where d is the interplanar spacing, which can be calculated using Bragg's law [9]:

$$n\lambda = 2d\sin\theta \tag{1}$$

X-rays with a specified wavelength (λ) and incidence angle (θ) can pass through a crystal or interact with specific atoms in the lattice. In reality, X-ray photons interact with the electron density around atoms to cause diffraction.

Rays reflected from the neighboring planes have a path difference of 2dsinθ. where d is the interplanar spacing, which can be computed using Bragg's law [10]:

$$d_{hkl} = \frac{a}{\sqrt{\frac{h^2+k^2}{a^2} + \frac{l^2}{c^2}}} \tag{2}$$

In this text, (a) and (c) refer to lattice parameters. This explains the conditions under which diffraction occurs in unit cells that contain atoms only at the corners. However, when atoms are situated at other positions (such as face centers and within the interior of unit cells in face-centered cubic (FCC) and body-centered cubic (BCC) structures), they act as additional scattering centers. This can lead to out-of-phase scattering at specific Bragg angles, resulting in the absence of certain diffracted beams that, according to Equation (2), should theoretically exist. For instance, in the BCC crystal structure, diffraction occurs only if the sum of the indices h, k, and l is even. In contrast, for the FCC structure, h, k, and l must be either all odd or all even for diffraction to occur [11].

The best method to investigate the change in the matrix structure is to evaluate the c/a ratio and the volume of the unit cell (V), which for:

tetragonal unit cell is

$$V = a^2c \tag{3}$$

1.2. Particle Size, dislocation density and lattice distortion:

The term "crystal size" refers to the dimensions of the tiny crystalline clusters that a material may contain. Microscopic crystals within these materials are called "nano crystals" or "crystallites," while larger particles may consist of aggregates formed from smaller crystals. Crystal size is commonly measured using X-ray diffraction (XRD) analysis. In XRD, "widening" refers to an increase in peak width on the diffraction curve, which is caused by

the interference of various factors affecting the diffraction distribution of the X-ray beam.

This can be calculated using the Scherrer equation.[11]:

$$D = \frac{0.9\lambda}{\beta \cos\theta} \tag{4}$$

The parameter β represents the broadening of the diffraction line, defined as the full width at half-maximum intensity (in radians) of the peak. where D denotes the particle size, θ is the diffraction angle, and λ is the X-ray wavelength. This formula was used to calculate the particle size of very small crystals by analyzing the observed width of their diffraction patterns. The dislocation density (δ) is defined as the length of the dislocation lines per unit volume of the crystal. It can be calculated using the following equation [12]

$$\delta = \frac{1}{D^2} \tag{5}$$

The lattice distortions (ε) is local lattice distortions in the body-centered tetragonal phase (β-Sn) matrix. values are calculated using the Williams and Hall formula [13] :

$$\frac{\beta \cos\theta}{\lambda} = \frac{1}{D} + \frac{2\varepsilon \sin\theta}{\lambda} \tag{6}$$

or :

$$\varepsilon = \frac{\beta D \cos\theta - \lambda}{2D \sin\theta} \tag{7}$$

1.3. The X-ray density (D_x) and the bulk density (D_b):

Understanding the crystal structure of a metallic solid can be helpful in calculating its density using the following equation [11]**:**

$$D_x = \frac{ZM_{\mathrm{wt}}}{N_A V} \tag{8}$$

where Z is the number of atoms per unit cell, M_wt is the molecular weight, V is the volume of the unit cell, and N_A is Avogadro's number.

Bulk density is the ratio of the weight of the compound to its volume.

$$D_b = \frac{m}{V} \tag{9}$$

where m ,V are the mass and the volume of the sample.

2. EXPERIMENTAL AND METHOD:

The Sn-Ag-Cu alloys were created using pure tin (Sn), silver (Ag), and copper (Cu) with a purity of 99.99% as the starting materials. A sensitive electronic balance with an accuracy of approximately 0.0001 grams was used to weigh the pure elements, as shown in Table (1). The five alloys were produced by melting the metals at a temperature of 750 degrees Celsius for two hours. They were then allowed to cool progressively to room temperature (RT) to achieve full phase precipitation. Finally, the collected samples were rolled and drawn.

After polishing the samples with silicon paper and cleaning them in a CH_3COCH_3 solution, they were annealed at $100 \pm 2°C$ for 6 h to eliminate any residual stress. Subsequently, the samples were allowed to cool slowly to room temperature at a rate of $1°C$ per minute. To investigate the changes in the microstructure with varying copper concentrations, the phases of the alloy samples were identified using X-ray diffraction (XRD). The analysis was performed using a Shimadzu XRD model EDX-720 at the Yemen Geological Survey and Mineral Resources Board (YGSMRB). This technique was employed to study the lattice characteristics and size of the crystalline unit cells. All samples were polished using a machine before analysis.

During the polishing procedure, the specimen was rinsed with hydrochloric acid to prevent contamination from coarser grit on its surface. After polishing with silicon paste, the X-ray diffraction (XRD) patterns of the materials were obtained using Cu Kα radiation (λ = 1.54056 $A°$) in the 2θ range of $5°$ to $75°$. The source operated at an accelerating voltage of 40 kV and tube current of 20 mA.

A continuous scan was performed at a constant rate of $0.02°$ per second. Figure (1) illustrates how X-rays of a specific wavelength are used to measure the intensity of the diffracted radiation while moving both the sample and detector. As the counter progresses at a constant angular velocity, the recorder automatically displays the intensity of diffracted beam, which was monitored by the counter, as a function of the diffraction angle (2θ). The X-ray counts at each stage were saved in a file on the computer. Following the measurement, the samples were washed with a CH_3COCH_3 solution [14].

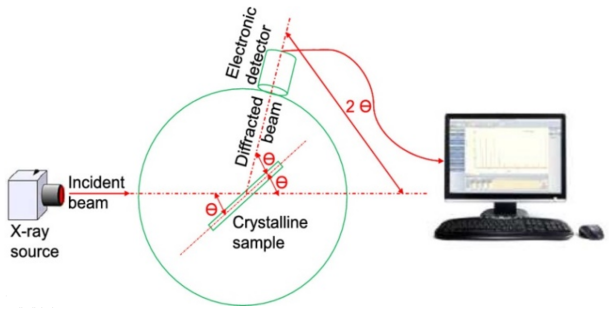

Figure 1. XRD instrument schematic

An incident X-ray beam shines on the surface and a film or electronic detector captures the signal as it completes an arc [15].

Scanning electron microscopy (SEM) is the technique of choice for analyzing specimen surfaces. Figure (2)

Table 1. Ternary alloy groups.

Solder alloy	Sn		Ag		Cu		Total	
	Mass (gm)	Percentage(%)	Mass (gm)	Percentage(%)	Mass (gm)	Percentage(%)	Mass (gm)	Percentage(%)
96.3Sn3.5Ag0.2Cu	96.3	96.3	3.5	3.5	0.2	0.2	100	100
96.1Sn3.5Ag0.4Cu	96.1	96.1	3.5	3.5	0.4	0.4	100	100
95.9Sn3.5Ag0.6Cu	95.9	95.9	3.5	3.5	0.6	0.6	100	100
95.7Sn3.5Ag0.8Cu	95.7	95.7	3.5	3.5	0.8	0.8	100	100
95.5Sn3.5Ag1Cu	95.5	95.5	3.5	3.5	1.0	1.0	100	100

shows the typical layout of an SEM, which encompasses an electron gun (electron source and accelerating anode), electromagnetic lenses to focus the electrons, a vacuum chamber housing the specimen stage, and a selection of detectors to collect the signals emitted from the specimen [16].

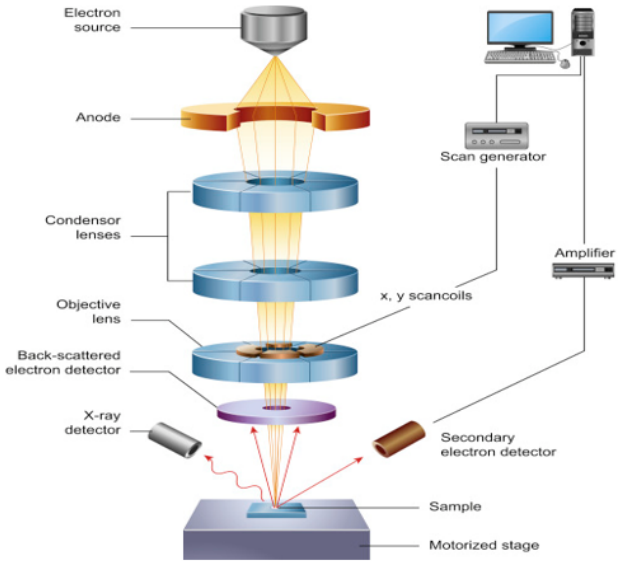

Figure 2. Schematic diagram of the core components of an SEM microscope Formatting Citation [16].

Microstructural characterization was performed using scanning electron microscopy (SEM) in the secondary electron imaging mode to obtain high-resolution topographical information of the sample surfaces. This technique relies on the detection of low-energy secondary electrons emitted from the sample surface owing to its interaction with the incident electron beam, typically within an energy range of approximately 3–5 eV, making it particularly sensitive to fine surface details.

The front detector grid voltage was set to 200 V to enhance the collection efficiency of the low-energy secondary electrons and improve the signal-to-noise ratio, thereby increasing the clarity of the resulting images. The scanning process was conducted using a raster of 1000 lines to generate images with dimensions of 10 × 10 cm, and operated at a refresh rate of 30 frames per second. This configuration ensured a balance between the spatial resolution and temporal stability during image acquisition.

Images were recorded using a cathode ray tube (CRT) equipped with a short-persistence phosphor screen, which helped minimize motion blur and improve image sharpness. This integrated setup enabled the acquisition of high-quality surface microstructural images, supporting a reliable and detailed analysis of the structural characteristics of the material [17].

3. RESULTS AND DISCUSSION:

3.1. Structural analysis

The X-ray diffraction patterns of the alloys listed in table reveal the following [17]: Copper influences both the intensity and position of all peaks in the Sn-3.5Ag alloy. Specifically, copper enhanced the peaks and shifted the 2θ angle. This suggests that the peaks in the Sn-3.5Ag alloy were modified. The observed shift in the diffracted lines may be attributed to the dissolution of copper atoms within the Sn-3.5Ag matrix [18].

Table (2a,b,c,d.e) summarizes the phases and crystal systems illustrated in Figure (3a-e). The figures demonstrate that increasing the copper concentration leads to a gradual increase in the peak strength, particularly at the 200 level. X-ray investigations revealed the presence of Ag_3Sn and Cu_6Sn_5 intermetallic compounds (IMCs) within the β-Sn matrix [19, 20].

The particle size (D) values of the $Sn–3.5Ag–Cu$ alloys were determined using the Scherrer formula (4). The curves in Figures (4-a and 4-b) represent the relationship between the crystalline size (D) and dislocation density (δ) in $Sn–3.5Ag–Cu$ alloys at different copper

Table (2-a): XRD pattern for 96.3Sn–3.5Ag–0.2Cu alloy.

No	2θ	d (nm)	Hkl	I%	FWHM	Crystallite size D (nm)	$\delta = \frac{1}{D^2}$ $(\times 10^{-7}\mathrm{nm}^{-2})$
1	30.566	0.215	(200)	84.4	0.117	70.3891721	2.01831
2	32.005	0.224	(101)	65.8	0.164	50.3935536	3.93777
3	43.406	0.301	(220)	19.3	0.151	56.6251614	3.11875
4	45.191	0.313	(211)	100	0.183	47.0207061	4.52295
5	55.613	0.380	(301)	35.3	0.126	71.280851	1.96813
6	64.991	0.437	(321)	40.5	0.162	58.1418841	2.95816
7	73.455	0.488	(411)	26.6	0.144	68.8327519	2.11062
Average						60.3834400	2.94781

Table (2-b):XRD pattern for 96.1Sn-3.5 Ag-0.4 Cu alloy.

No	2θ	d (nm)	Hkl	I%	FWHM	Crystallite size D (nm)	$\delta = \frac{1}{D^2}$ $(\times 10^{-7}\mathrm{nm}^{-2})$
1	31.257	0.219	(2 0 0)	100	0.253	32.6058324	9.4061
2	32.869	0.230	(1 01)	53.3	0.163	50.8140383	3.87287
3	45.767	0.317	(211)	54.1	0.28	30.796201	0.54401
4	56.246	0.384	(301)	24	0.178	50.6054296	3.90486
5	64.711	0.436	(400)	17.3	0.135	69.6620479	2.06067
6	65.632	0.442	(321)	43.9	0.252	37.5111644	7.10688
7	73.866	0.490	(411)	23.4	0.191	52.0344326	3.69333
Average						46.2898780	4.369817

(Cu) concentrations, as presented in 3. The average crystalline size initially increased with the addition of copper, followed by a sudden decrease at higher Cu levels. This behavior can be attributed to the homogeneous distribution and dynamic movement of atoms within the alloy matrix, which is influenced by the specific elemental composition of the alloy.

To further assess the microstructural characteristics of these alloys, the dislocation density (δ) was evaluated. The dislocation density serves as a key parameter that indicates the degree of defects within the crystal lattice. It is defined as the total length of the dislocation lines per unit volume of the crystal. The dislocation density values for the $\mathrm{Sn–3.5Ag–Cu}$ alloys were calculated using Equation (5), and the results are summarized in Table (3). Figure (4-b) illustrates the relationship between dislocation density and copper content.

The X-ray diffraction (XRD) results of the $(96.5 - x)\,\mathrm{Sn} - 3.5\,\mathrm{Ag} - x\,\mathrm{Cu}$ solder alloys revealed a complex and non-uniform evolution of the crystal structure with increasing Cu content. The observed shifts in the diffraction peak positions, together with variations in the interplanar spacing (d-spacing), indicate significant lattice distortion within the β-Sn matrix.

This behavior is consistent with previously reported findings on Sn–Ag–Cu solder systems, where the addition of Cu leads to lattice strain and promotes the formation of intermetallic compounds such as $\mathrm{Cu_6Sn_5}$ and $\mathrm{Ag_3Sn}$, which strongly influence the diffraction response and phase stability. This result is consistent with that of Lau et al. [21]. The present results show a nonlinear variation in the lattice parameters with the Cu content, indicating that the structural response is anisotropic rather than isotropic. The a-axis is more sensitive to Cu incorporation, whereas the c-axis remains relatively stable, reflecting the directional rigidity of the β-Sn lattice. This anisotropic lattice distortion is commonly associated with atomic size mismatches and solid-solution effects in Sn-based alloys.

Furthermore, the variation in the d-spacing was not uniform across all crystallographic planes (hkl). Some reflections exhibited a decrease in d-spacing (shift toward higher 2θ angles), whereas others showed the opposite trend. This mixed behavior suggests the coexistence of competing mechanisms, including the partial solid solution formation of Cu in β-Sn, lattice strain accumulation, and the development of intermetallic phases such as $\mathrm{Cu_6Sn_5}$ and $\mathrm{Ag_3Sn}$ at higher Cu concentrations. This

Table (2-c): XRD pattern for 95.9Sn-3.5Ag-0.6Cu alloy.

No	2θ	d (nm)	Hkl	I%	FWHM	Crystallite size D (nm)	$\delta = \frac{1}{D^2}$ $(\times 10^{-7} \mathrm{nm}^{-2})$
1	30.722	0.290	(200)	100	0.22	37.44820661	7.1308
2	32.081	0.278	(101)	25.3	0.186	44.44148865	5.06317
3	43.831	0.206	(220)	1.73	0.187	45.79197123	4.76893
4	44.979	0.201	(211)	73.4	0.24	35.82576638	7.79128
5	55.478	0.165	(301)	15.6	0.233	38.52281836	6.73851
6	62.578	0.148	(112)	3.03	0.191	48.6720728	4.22124
7	63.921	0..145	(400)	16.5	0.144	65.02571172	2.36499
8	64.6591	0.144	(321)	9.31	0.477	19.71002047	25.74103
Average						41.92973946	7.977493

Table (2-d): XRD pattern for 95.7Sn-3.5Ag-0.8Cu alloy.

No	2θ	d (nm)	Hkl	I%	FWHM	Crystallite size D (nm)	$\delta = \frac{1}{D^2}$ $(\times 10^{-7} \mathrm{nm}^{-2})$
1	31.199	0.290	(200)	73.8	0.289	28.5401689	12.27685
2	32.581	0.278	(101)	64.3	0.237	34.9222727	8.19964
3	44.442	0.265	(220)	22.3	0.23	37.311431	7.18317
4	45.47	0.201	(211)	100	0.273	31.5514377	10.04527
5	55.786	0.165	(301)	32.5	0.164	54.8082569	3.32896
6	63.098	0.148	(112)	9.52	0.258	36.1324461	7.65959
7	64.423	0.145	(400)	10.8	0.118	79.5716602	1.57937
8	65.229	0.143	(321)	32.3	0.331	28.4939055	12.31675
9	73.808	0.129	(411)	27.3	0.146	68.046561	21.5967
Average						44.3753489	9.354033

Table (2-e): XRD pattern for 95.5Sn-3.5Ag-1Cu alloy.

No	2θ	d (nm)	Hkl	I%	FWHM	Crystallite size D (nm)	$\delta = \frac{1}{D^2}$ $(\times 10^{-7} \mathrm{nm}^{-2})$
1	31.199	0.219	(200)	72.3	0.289	28.5401689	12.27685
2	32.581	0.228	(101)	58	0.237	34.9222727	8.19964
3	45.47	0.315	(211)	100	0.273	31.5514377	10.04527
4	55.786	0.381	(301)	24.9	0.164	54.8082569	3.32896
5	63.098	0.426	(112)	21.9	0.258	36.1324461	7.65959
6	64.423	0.434	(400)	21.7	0.118	79.5716602	1.57937
7	65.229	0.439	(321)	55.6	0.331	28.4939055	12.31675
8	73.808	0.489	(411)	45.9	0.146	68.046561	2.15967
Average						45.2585286	7.195762

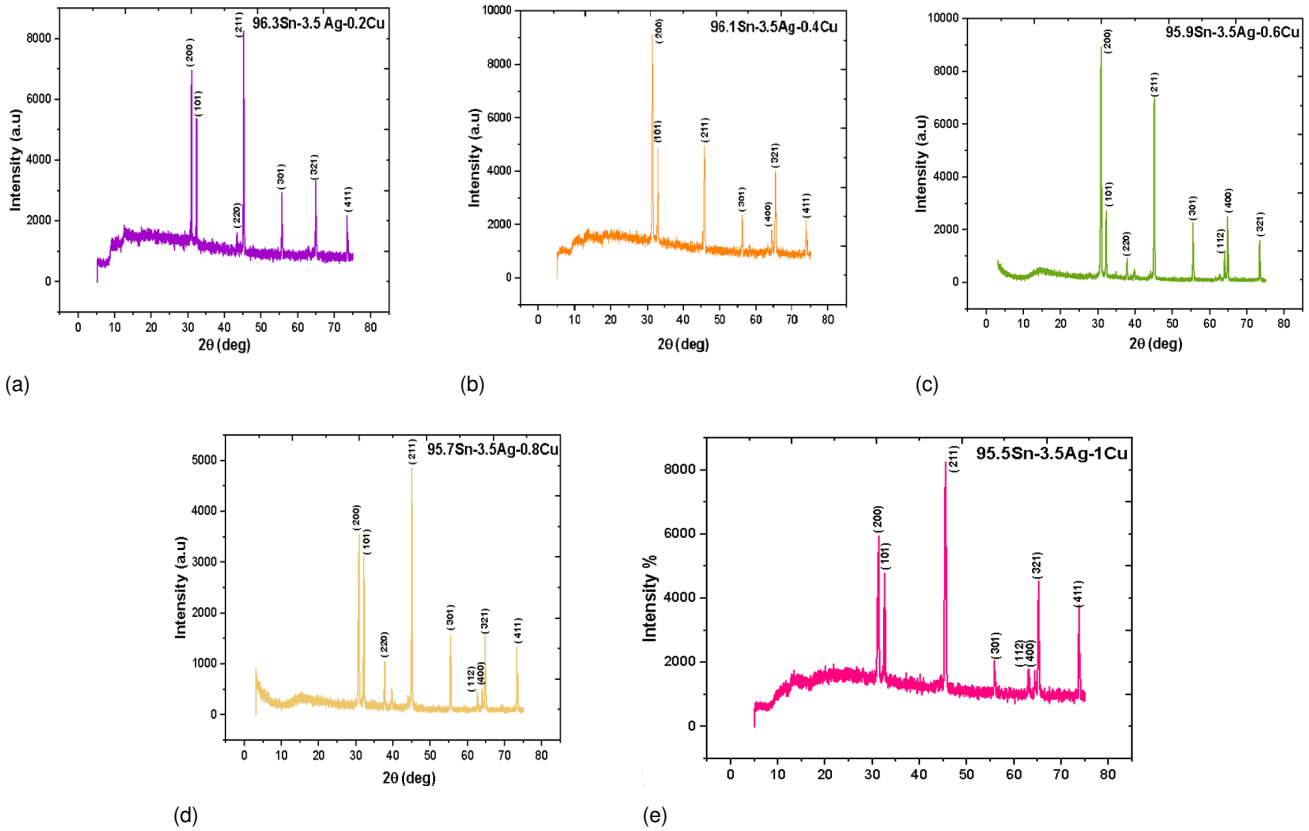

Figure 3. (a-e) XRD pattern for all alloys.

Table 3. The Crystalline size(D) and Dislocation density alloys.

Samples wt.%	Crystalline size(D) (nm)	Dislocation density (δ) $\times 10^{-7}$ $(nm)^{-2}$
96.3Sn3.5Ag0.2Cu	60.38	2.95
96.1Sn3.5Ag0.4Cu	46.29	4.37
95.9Sn3.5Ag0.6Cu	41.93	7.98
95.7Sn3.5Ag0.8Cu	44.38	9.35
95.5Sn3.5Ag1Cu	45.26	7.19

result is consistent with that of Sharma et al. [22].

The increasing Cu content enhances lattice distortion owing to the atomic size mismatch between Cu and Sn, generating local stress fields that contribute to peak broadening and irregular shifts. Such microstructural evolution has been widely reported in lead-free solder systems, where phase formation and solubility limits govern the overall structural stability and diffraction behavior [23].

The results shown in Figure (4-b) and Table (3) indicate that the dislocation density increases with increasing copper content. This behavior is associated with the reduction in crystallite size, which increases the number of particle boundaries acting as barriers to dislocation movement within the lattice.

When the copper content increased from 0.6% to 1%, a slight increase in the crystalline size was observed.

observed, ranging from 41.93 nm to approximately 45.26 nm. This change is attributed to the growth of larger crystals at the expense of smaller ones, leading to partial coarsening of the microstructure.

Table (4) shows that increasing the copper concentration leads to a decrease in the unit cell volume because the copper atom is smaller than the tin (Sn) atom, causing contraction of the crystal lattice.

The predominant phase remained β-Sn (body-centered tetragonal structure), consistent with the findings of Al-Hammadi et al. [23, 24].

3.2. The X-ray density(D_x) and bulk density (D_B):

Table (4) presents the density measurement results for various solder alloys and basic solder. The theoretical density of $\mathrm{Sn-3.5Ag-0.2Cu}$ solder ranges from 4.7 to 7.4 g cm^{-3} Because copper has a higher density than tin

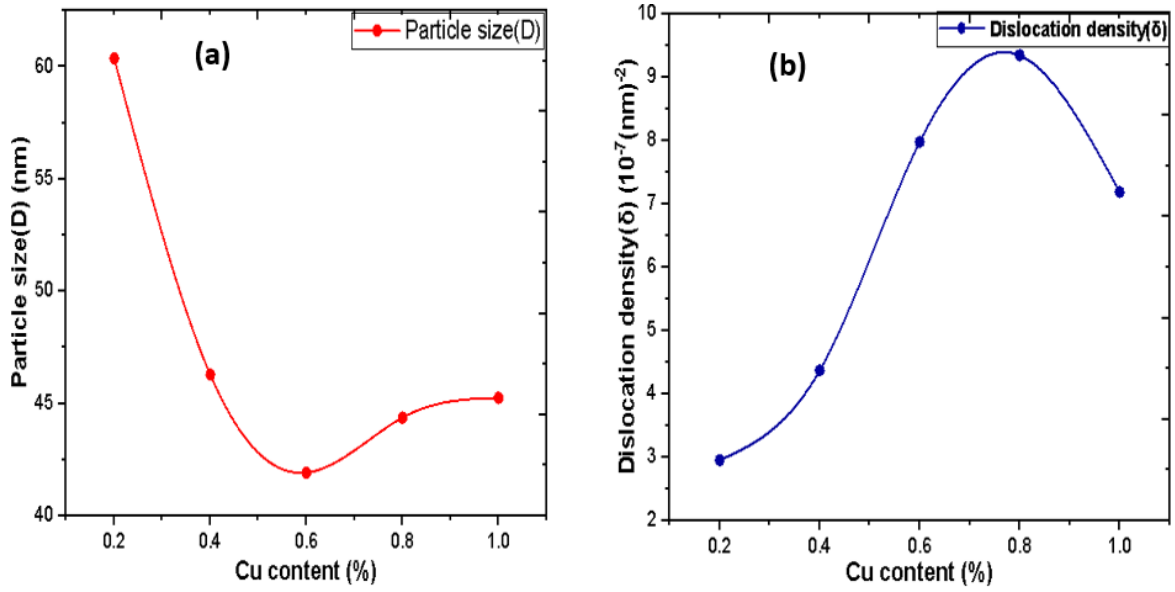

Figure 4. (4- a) The variation in particle size values of Sn-3.5Ag with Cu –content, (4-b) The variation in dislocation density values with Cu -content.

but a lower density than silver, increasing the percentage of copper in the alloy leads to a slight increase in the overall density of the alloy, as illustrated in Figure (5) [25]. The density calculated from X-ray diffraction (XRD) analysis is considered more accurate than the bulk density; therefore, the apparent increase in the bulk density may be associated with experimental uncertainties or measurement errors.

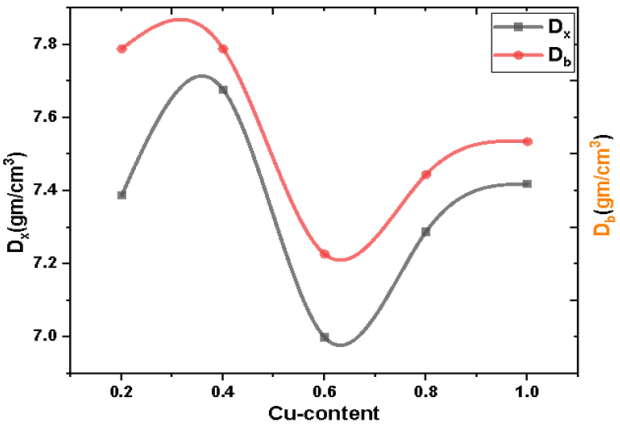

Figure 5. The X-ray density (D_x) and bulk density (D_b) as a function of Cu Content.

X-ray diffraction (XRD) analysis revealed that Cu incorporation altered the lattice parameters while maintaining the dominant β-Sn tetragonal phase. The changes in the lattice constants a and c, with only slight variations in the axial ratio (c/a), indicate lattice distortion governed by atomic substitution and strain accommodation.

These changes arise from the atomic size mismatch between Cu and Sn. Because Cu has a smaller atomic radius, its incorporation generates a localized strain within the β-Sn lattice. Due to the anisotropic nature of the tetragonal structure, strain relaxation occurs mainly along the a-axis, while the c-axis remains comparatively resistant to deformation, explaining the limited variation in the c/a ratio [25].

Cu addition also promotes stabilization through the formation of thermodynamically stable intermetallic compounds, particularly Cu_6Sn_5, which reduces compositional heterogeneity and acts as pinning centers that restrict grain boundary migration. This effect limits grain growth and promotes microstructural refinement, which is associated with improved mechanical reliability of the material.

At the atomic scale, Cu enhances the bonding strength within the lattice owing to its higher cohesive energy relative to that of Sn, reducing atomic mobility and increasing structural stability without causing phase transformation.

The maximum axial ratio was observed at 1 wt. % Cu suggests an optimal alloying level where lattice distortion and stabilization are balanced; higher Cu contents may introduce competing strain fields and excess intermetallic formation that disturb lattice coherence [26].

Overall, Cu acts as a reinforcing element through lattice distortion, anisotropic strain redistribution, and intermetallic stabilization while maintaining the integrity of the β-Sn phase and improving the alloy performance [27].

3.3. SEM ANALYSIS:

The scanning electron microscope (SEM) was employed to investigate the microstructure of Sn–3.5Ag–Cu alloys at various copper concentrations. The images revealed three main regions: the gray β-Sn phase, which formed

Table 4. The X-ray density (D_x)and bulk density(D_b).

Samples	Cu addition %	a (nm)	c (nm)	(c/a) (nm)	D_x (gm/cm^3)	D_b (gm/cm^3)
96.3Sn3.5Ag	0.2	0.57829	0.3178	0. 54955	7.388	7.7891
96.1Sn3.5Ag	0.4	0.56887	0.31576	0. 55506	7.677	7.7887
95.9Sn3.5Ag	0.6	0.58124	0.317693	0. 54657	7.00	7.2274
95.7Sn3.5Ag	0.8	0.58088	0.318387	0. 54581	7.2884	7.445
95.5Sn3.5Ag	1	0.57144	0.31863	0.557591	7.419	7.5351

the primary matrix of the alloys; the Cu_6Sn_5 intermetallic compounds, which appeared as small platelets or columns distributed within the eutectic regions and along the β-Sn grain boundaries; and the fine AgSn needles embedded within the eutectic areas. Both Cu_6Sn_5 and AgSn play crucial roles in strengthening the alloys and enhancing uniformity of the eutectic network, whereas the distribution of β-Sn highlights the effect of copper concentration on grain refinement and the overall improvement of the alloys' microstructure [28].

Figure (6-a) illustrates the microstructure characterized by relatively coarse β-Sn grains surrounded by dark eutectic regions. These eutectic areas contain fine needle-like Ag_3Sn intermetallic compounds, in addition to small Cu_6Sn_5 platelets distributed along the β-Sn grain boundaries and within the eutectic matrix. The overall morphology reflects a typical near-eutectic Sn-3.5Ag-Cu microstructure with limited Cu_6Sn_5 formation at this concentration. This result is in agreement with Jang et al [29, 30]

Figure (6-b) shows a noticeable refinement of the β-Sn grains, accompanied by an increased number of Cu_6Sn_5 platelets within the eutectic regions. The intermetallic compounds began to localize in specific regions, appearing as short columnar features.

This observation suggests a more effective incorporation and distribution of Cu within the Sn-rich matrix [31].

In Figure (6-c), further grain refinement of β-Sn is evident, along with a higher density of Cu_6Sn_5 intermetallic compounds in the eutectic regions. The Ag_3Sn phase maintains its needle-like morphology and remains uniformly distributed between the β-Sn grains and the eutectic areas. Meanwhile, Cu_6Sn_5 appears as finer and more regularly shaped platelets, indicating enhanced microstructural homogeneity.

Figure (6-d) demonstrates continued refinement of the β-Sn grains. The Cu_6Sn_5 platelets become more widely dispersed throughout the eutectic structure and exhibit a more uniform and organized morphology compared to alloys with lower Cu content. This suggests an increasing role of Cu in modifying the eutectic network [29].

Finally, Figure (6-e) reveals that the β-Sn grains reach their minimum observed size, while the eutectic regions become significantly enriched with Cu_6Sn_5 intermetallic compounds, which appear as well-defined columnar and platelet-like structures. The Ag_3Sn needles remain embedded within the eutectic matrix. Overall, the progressive increase in Cu content promotes grain refinement, enhances the formation and uniform distribution of Cu_6Sn_5 intermetallic compounds, and contributes to the strengthening and stabilization of the eutectic network within the alloy system [26].

The refinement of β-Sn grains with increasing copper content can be interpreted based on the role of Cu in the nucleation and growth mechanisms during solidification. An increase in Cu concentration enhances the probability of forming new Cu_6Sn_5 intermetallic nuclei during the crystallization stage. These nuclei act as heterogeneous nucleation sites, which restrict the excessive growth of β-Sn grains. Consequently, the nucleation density increases while the growth time decreases, resulting in a finer and more homogeneous microstructure.

Moreover, increasing the Cu content promotes the formation of Cu_6Sn_5 intermetallic compounds within the eutectic regions. This compound modifies the eutectic morphology, transforming it from a relatively irregular distribution at lower concentrations to a more uniform and interconnected network at higher Cu contents. This behavior can be attributed to the improved distribution of Cu within the Sn-rich matrix, which reduces local compositional gradients and enhances microstructural homogeneity. Furthermore, the progressive and enhancing the structural performance of Sn-3.5Ag-Cu alloys.

This behavior can be interpreted as a transition in the solidification mechanism from a growth-controlled regime at low copper concentrations, where grain evolution is dominated by unrestricted β-Sn growth, to a nucleation-controlled regime at higher copper contents, where enhanced formation of Cu_6Sn_5 intermetallic compounds provides effective heterogeneous nucleation sites. This transition occurs in parallel with the development of diffusion-controlled growth of Cu_6Sn_5 phases, in which atomic diffusion governs the formation rate and spatial distribution of the intermetallic compounds. Collectively, these mechanisms lead to improved eutectic structural homogeneity and significant grain refinement. This result is in agreement with M. Abtew et al. [32].

The XRD results revealed the presence of three phases (β-Sn, Ag_3Sn, and Cu_6Sn_5), and calculations

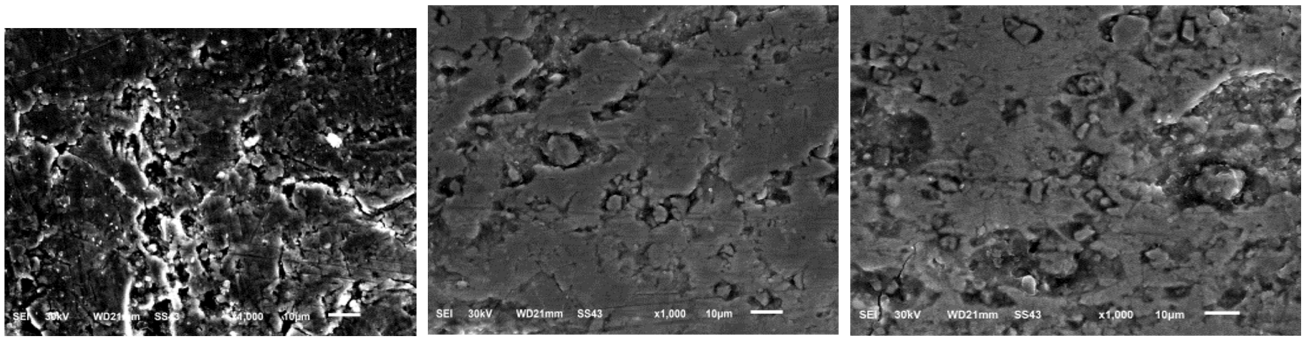

(a) SEM images 96.3Sn-3.5 Ag-0.2Cu alloy. **(b)** SEM image for 96.1Sn-3.5 Ag-0.4 Cu alloy. **(c)** SEM image for 95.9Sn-3.5Ag-0.6Cu alloy.

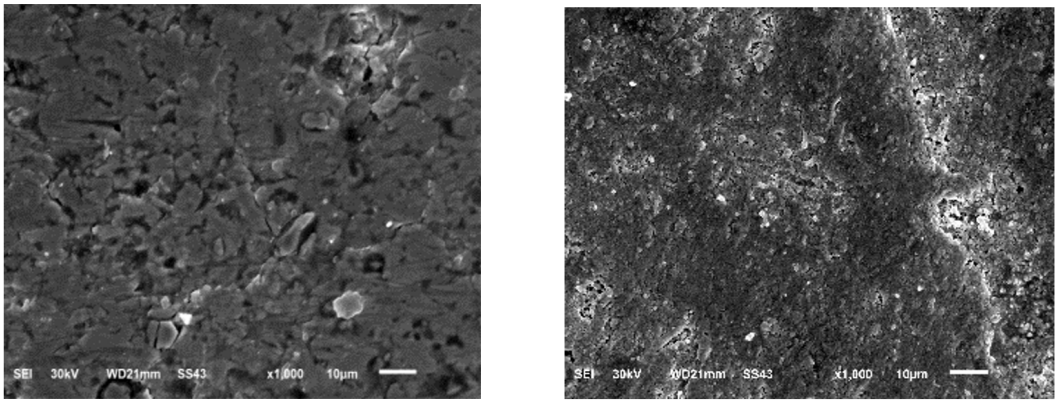

(d) SEM image for 95.7Sn-3.5Ag-0.8Cu alloy. **(e)** SEM image for 95.5Sn-3.5Ag-1Cu alloy.

Figure 6. (a-e) XRD pattern for all alloys.

indicated that the crystallite size was smaller than the particle size measured by SEM, suggesting the polycrystalline nature of

the formed particles. This implies that each microscopically observed particle consists of multiple crystallites. This result is consistent with that of Cullity et al. [33].

Accordingly, the refinement of the crystallite size, as determined by XRD, was consistent with the increase in the particle size measured by SEM.

4. CONCLUSION :

1. X-ray diffraction (XRD) analysis shows that this method effectively detects crystalline phases in Sn-3.5Ag-xCu alloys. The investigation revealed that all of the produced alloys exhibited a tetragonal structure. Copper dissolves into the tin-silver matrix, resulting in variations in peak intensities and shifts in the 2θ angle. The peak intensities of intermetallic compounds, such as Ag_3Sn and Cu_6Sn_5, indicate changes in the microstructure of the alloys.

2. Increasing the copper concentration reduced the volume of the unit cell while maintaining the dominant phase, β-Sn. Changes in the (c/a) ratio were observed as the copper content increased gradually.

3. The ratio increased with the addition of copper, reaching its highest value at 1% Cu.

4. The theoretical density of the Sn-3.5 Ag-Cu alloy ranged from 7.4 g/cm³ to 4.7 g/cm³. The overall density of the alloy increased slightly with increasing copper concentration.

5. It was demonstrated that the gradual increase in copper content in the Sn-3.5Ag-Cu alloy leads to a pronounced refinement of the β-Sn grains, along with enhanced formation and a more uniform and interconnected distribution of Cu_6Sn_5 intermetallic compounds within the eutectic regions. This behavior is attributed to the role of copper in promoting heterogeneous nucleation during solidification, which increases the nucleation density and restricts grain growth, resulting in a finer and more homogeneous microstructure.

The XRD results also revealed the presence of the phases (β-Sn, Ag_3Sn, and Cu_6Sn_5) and indicated that the crystallite size was smaller than the particle size measured by SEM, confirming the polycrystalline nature of the formed particles. Accordingly, controlling the copper content is considered a critical factor for improving the microstructure and enhancing the mechanical properties of Sn-3.5Ag-Cu alloys.

REFERENCES

[1] M. L. Huang and L. Wang, “Effects of cu, bi, and in on microstructure and tensile properties of sn-ag-x (cu, bi, in) solders,” *Metall. Mater. Trans. A*, vol. 36, no. 6, pp. 1439–1446, 2005. DOI: 10.1007/s11661-005-0236-7.

[2] S. Li, Y. Zhang, and X. Liu, "Corrosion behavior of sn-based lead-free solder alloys: A review," *J. Mater. Sci. Mater. Electron.*, vol. 31, no. 10, pp. 9076–9090, 2020. DOI: 10.1007/s10854-020-03670-2.

[3] A. Al-Hammadi, F. Ghailan, and F. A. Hulaiqah, "Effect of melting at different temperatures on the structure and mechanical properties of solder alloy (sn–ag–in)," *Albaydha Univ. J.*, vol. 3, pp. 161–181, 2021.

[4] M. Ghaleeh, A. Baroutaji, and M. A. Qubeissi, "Microstructure, isothermal and thermomechanical fatigue behaviour of leaded and lead-free solder joints," *Eng. Fail. Anal.*, vol. 117, p. 104 846, 2020. DOI: 10.1016/j.engfailanal.2020.104846.

[5] Q. V. Bui, N. D. Nam, B. I. Noh, A. Kar, J. G. Kim, and S. B. Jung, "Effect of ag addition on the corrosion properties of sn-based solder alloys," *Mater. Corros.*, vol. 61, no. 1, pp. 30–33, 2010. DOI: 10.1002/maco.200905237.

[6] D. Kumar, S. Idapalapati, W. Wang, and S. Narasimalu, "Effect of surface mechanical treatments on the microstructure-property-performance of engineering alloys," *Materials*, vol. 12, no. 16, p. 2503, 2019. DOI: 10.3390/ma12162503.

[7] H. S. Mohamed, M. M. Mostafa, and N. M. Mahmoud, "Crystallographic, microstructure, electrical, and hardness characterization of advanced sn-9zn-0.5zro2 and sn-9zn-xni lead-free solder alloys," *J. Mater. Sci. Mater. Electron.*, vol. 36, no. 13, pp. 1–20, 2025. DOI: 10.1007/s10854-025-14760-9.

[8] M. S. N. Al-Salmi, G. N. A. A. M. A., S. Alsowidy, and A. T. Naji, "Silver (ag) improvements on the structural, creep resistance and electrical conductivity properties of eutectic sn–9zn alloys," *Albaydha Univ. J.*, vol. 2, no. 3, pp. 142–155, 2021. DOI: 10.56807/buj.v2i3.116.

[9] L. Sun and L. Zhang, "Properties and microstructures of sn–ag–cu–x lead-free solder joints in electronic packaging," *Adv. Mater. Sci. Eng.*, vol. 2015, no. 1, p. 639 028, 2015. DOI: 10.1155/2015/639028.

[10] J. Epp, "X-ray diffraction (xrd) techniques for materials characterization," in *Materials Characterization Using Nondestructive Evaluation (NDE) Methods*, Elsevier, 2016, pp. 81–124.

[11] B. S. Mitchell, *An Introduction to Materials Engineering and Science for Chemical and Materials Engineers*. Hoboken, NJ, USA: John Wiley & Sons, 2003.

[12] B. E. Warren, *X-ray Diffraction*. Mineola, NY, USA: Courier Corporation, 1990.

[13] M. Dhanam, R. R. Prabhu, and P. K. Manoj, "Investigations on chemical bath deposited cadmium selenide thin films," *Mater. Chem. Phys.*, vol. 107, no. 2–3, pp. 289–296, 2008. DOI: 10.1016/j.matchemphys.2007.07.048.

[14] G. K. Williamson and W. H. Hall, "X-ray line broadening from filed aluminium and tungsten," *Acta Metall.*, vol. 1, no. 1, pp. 22–31, 1953. DOI: 10.1016/0001-6160(53)90006-6.

[15] A. H. Al-Hammadi et al., "An investigation on the structural, morphological, optical, and antibacterial activity of sr:cus nanostructures," *Sci. Reports*, vol. 14, no. 1, 2024. DOI: 10.1038/s41598-024-73701-4.

[16] N. Brodusch, H. Demers, and R. Gauvin, *Field Emission Scanning Electron Microscopy: New Perspectives for Materials Characterization*. Cham, Switzerland: Springer, 2017.

[17] H. Khan, A. S. Yerramilli, A. D'Oliveira, T. L. Alford, D. C. Boffito, and G. S. Patience, "Experimental methods in chemical engineering: X-ray diffraction spectroscopy—xrd," *Can. J. Chem. Eng.*, vol. 98, no. 6, pp. 1255–1266, 2020. DOI: 10.1002/cjce.23747.

[18] F. I. Hussain, "Synthesis of nano compound ($ba_{1-x}sr_xtio_3$) by sol–gel method and study of its structural properties," *Ibn Al-Haitham J. for Pure Appl. Sci.*, vol. 29, no. 1, 2016.

[19] K. Gain and L. Zhang, "Temperature and humidity effects on microstructure and mechanical properties of an environmentally friendly sn–ag–cu material," *J. Mater. Sci.*, vol. 54, pp. 12 863–12 874, 2019. DOI: 10.1007/s10853-019-03787-2.

[20] M. I. I. Ramli et al., "Formation and growth of intermetallic compounds in lead-free solder joints: A review," *Materials*, vol. 15, no. 4, pp. 1–20, 2022. DOI: 10.3390/ma15041451.

[21] J. H. Lau and N. C. Lee, *Electronics Manufacturing with Lead-Free, Halogen-Free, and Conductive-Adhesive Materials* (Springer Series in Materials Science). Springer, 2003, vol. 71, pp. 1–500. DOI: 10.1007/978-1-4757-3763-4.

[22] P. Sharma and Y. C. Chan, "Lead-free solder interconnections," *Acta Materialia*, vol. 53, no. 8, pp. 2351–2360, 2005. DOI: 10.1016/j.actamat.2004.11.028.

[23] S. Alsowidy, A. M. Aljarbani, and M. S. Gumaan, "Microstructural and creep characterization of sn-0.7cu and sn-0.7cu-xbi lead-free solders for low cost electronic applications," *Results Mater.*, vol. 16, p. 100 319, 2022. DOI: 10.1016/j.rinma.2022.100319.

[24] A. Al-Hammadi, I. G. Loqman, and R. Al-Hdhrami, "Mechanical properties of the (81sn–xcu–(19–x)in)% alloys with x = 1, 2, 3, 4, and 5," *Sana'a Univ. J. Appl. Sci. Technol.*, vol. 1, pp. 189–198, 2023.

[25] Z. Yao, Y. Zhang, L. Chen, and X. Liu, "Effect of cu addition on the microstructure and mechanical properties of sn-58bi-0.5ag solder alloys," *J. Electron. Mater.*, vol. 51, no. 8, pp. 4567–4576, 2022. DOI: 10.1007/s11664-022-09601-y.

[26] Y. Li, H. Zhang, and Q. Wang, "Effects of alloying additions on lattice characteristics in sn-3.0ag-0.5cu solder investigated by in-situ x-ray diffraction," *J. Mater. Sci. Mater. Electron.*, vol. 37, no. 4, pp. 1–10, 2026. DOI: 10.1007/s10854-026-16641-1.

[27] R. Sayyadi and H. Naffakh-Moosavy, "Physical and mechanical properties of synthesized low ag/lead-free sn–ag–cu–xbi (x = 0, 1, 2.5, 5 wt%) solders," *Mater. Sci. Eng. A*, vol. 735, pp. 367–377, 2018. DOI: 10.1016/j.msea.2018.08.056.

[28] M. Reid, J. Punch, M. Collins, and C. Ryan, "Effect of ag content on the microstructure of sn–ag–cu based solder alloys," *Solder. Surf. Mt. Technol.*, vol. 20, no. 3, pp. 20–26, 2008. DOI: 10.1108/09540910810902651.

[29] K. N. Tu and K. Zeng, "Interfacial reactions between lead-free solders and common base materials," *Mater. Sci. Eng. R: Reports*, vol. 34, no. 1–3, pp. 1–58, 2001. DOI: 10.1016/S0927-796X(01)00029-8.

[30] J. W. Jang, J. K. Lin, and D. R. Frear, "Effect of cu content on microstructure evolution of sn–ag–cu solder," *Metall. Mater. Trans. A*, vol. 36, no. 6, pp. 1439–1446, 2005. DOI: 10.1007/s11661-005-0236-7.

[31] T. Laurila, V. Vuorinen, and J. Kivilahti, "Interfacial reactions between lead-free solders and common base materials," *Mater. Sci. Eng. R: Reports*, vol. 49, no. 1–2, pp. 1–60, 2005. DOI: 10.1016/j.mser.2005.03.001.

[32] M. Abtew and G. Selvaduray, "Lead-free solders in microelectronics," *Mater. Sci. Eng. R: Reports*, vol. 27, no. 5–6, pp. 95–141, 2000. DOI: 10.1016/S0927-796X(00)00010-3.

[33] B. D. Cullity and S. R. Stock, *Elements of X-ray Diffraction*, 3rd ed. Upper Saddle River, NJ, USA: Prentice Hall, 2014.